Earth, Planets and Space
a SpringerOpen Journal

FULL PAPER Open Access

New perspectives on thermosphere tides: 1. Lower thermosphere spectra and seasonal-latitudinal structures

Alexander O Truskowski, Jeffrey M Forbes*, Xiaoli Zhang and Scott E Palo

Abstract

Thermosphere-Ionosphere-Mesosphere Energetics and Dynamics/Sounding of the Atmosphere using Broadband Emission Radiometry (TIMED/SABER) temperature measurements at 110 km and between ±50° latitude extending from 2002 through 2010 are analyzed to reveal the tidal spectrum entering the ionosphere-thermosphere (IT) system. Seasonal-latitudinal structures are presented for the most prominent spectral components which include DE3, DE2, D0, DW1, DW2, SE1 to SE4, SW1 to SW4, SW6, TE1, TW4, TW5, and TW7. Referring to recent calculations of lower atmosphere heat sources as well as vertical structure characteristics of these waves anticipated from classical tidal theory, we analyze the likely origins of these waves and the nature of their seasonal-latitudinal structures. Several waves are likely to arise through nonlinear wave-wave interactions, and in some cases, this appears to be the sole viable mechanism leading to their existence. The tidal spectrum quantified here is especially relevant to the dynamo generation of electric fields which then impose the tidal variability on the overlying F-region ionosphere. Part 2 of this 2-part study examines penetration of the tidal spectrum to the upper thermosphere.
Please see related article: http://www.earth-planets-space.com/content/66/1/122

Keywords: Tides; Thermosphere; Dynamics; Propagation

Background

The importance of atmospheric tides as drivers of thermosphere and ionosphere variability is now widely accepted. Of particular importance to the ionosphere are the tidal components that characterize the E-region (ca. 100 to 150 km) where the dynamo action of tidal winds generate electric fields. These electric fields map along equipotential magnetic field lines and drive E × B plasma drifts in the F-region (ca. 150 to 1,000 km), thus imposing the temporal and spatial variability of the E-region tides on the F-region plasma [e.g., (Jin et al. 2008; Kil et al. 2007, 2008, Lin et al. 2007; Liu and Watanabe 2008)]. Some part of the tidal spectrum producing electric fields originates *in situ* from the absorption of EUV radiation. Additional E-region tidal components propagate upward from sources in the troposphere and stratosphere, and a subset of these propagates into the upper thermosphere [ca. 400 km, (Forbes et al. 2009; Hagan et al. 2009; Haüsler and Lühr 2009; Oberheide and Forbes 2008) and exerts their influence on the ionospheric plasma through wind transport and composition changes (England et al. 2010; He et al. 2011; Immel et al. 2006, 2009). All of this variability competes with other meteorological influences, geomagnetic activity, and solar flux changes to produce the ionospheric variability that undermines operation of various communications and navigation systems. The neutral density variability produced by atmospheric tides also contributes significantly to uncertainty in satellite orbit and reentry predictions. These are just a few of the space weather problems that challenge our 21st century society.

The above scientific discoveries and their practical implications underscore the importance of knowing the spectrum of waves entering the ionosphere-thermosphere (IT) system from below. Forbes et al. 2008 provided some limited insights into variability of the tidal spectrum extending into the dynamo region, concentrating mainly on the equator and the height-latitude structures of a few major tidal components during particular months.

*Correspondence: forbes@colorado.edu
Department of Aerospace Engineering Sciences, University of Colorado, 1111 Engineering Dr., Boulder, CO 80309, USA

That study employed Sounding of the Atmosphere using Broadband Emission Radiometry (SABER) temperature measurements from the Thermosphere-Ionosphere-Mesosphere Energetics and Dynamics (TIMED) spacecraft between 2002 and 2006. In the present paper, we provide a more in-depth and complete analysis of the tidal spectrum entering the IT system from below, based on SABER measurements covering the period 2002 through 2010. In particular, we focus on seasonal-latitudinal structures and reveal several tidal components not highlighted in (Forbes et al. 2008) due to the more equatorial focus of that study.

Although the SABER instrument is still taking high-quality measurements, the 2002 to 2010 time period is chosen to maintain consistency with the complementary CHAMP and GRACE data analyzed in part 2 of this study, which examines penetration to the upper thermosphere of the tidal spectrum revealed in part 1. In particular, our goal in these papers is to point out the importance of certain components that have received little or no attention in the literature, thus significantly expanding our knowledge while at the same time raising new questions about their origins. Our results should prove useful for future studies that seek to establish whether tidal variability is responsible for other aspects of atmosphere-ionosphere system variability.

In addition to delineating the spectrum of tidal components at 110 km as a second objective of this study, we seek to explain the origins of the waves and the nature of their seasonal-latitudinal structures. We first examine recent estimates of tropospheric tidal heating to establish what waves might plausibly arise from this source. Classical tidal theory is also employed to estimate vertical wavelengths and thereby the relative susceptibility of various tidal components to dissipative filtering and trapping by the background thermal structure prior to reaching 110 km. The relevant background information is introduced in the 'The nature and origins of tides entering the thermosphere' section and applied to the observed tidal spectrum in the 'Results and discussion' section. The data and processing steps are briefly summarized in the 'Data and tidal analysis method' section. In the 'Conclusions' section, we summarize our results and furthermore consider what components of the tidal spectrum might arise from nonlinear wave-wave interactions.

Methods

The nature and origins of tides entering the thermosphere

Throughout this paper as well as part 2, we employ the following mathematical description of a tidal oscillation, consistent with the periodicity in time and longitude imposed by the Earth's rotation with respect to the Sun:

$$A_{n,s}\cos\left(n\Omega t + s\lambda - \phi_{n,s}\right) \tag{1}$$

The temporal periodicity is represented by the rotation rate of the Earth, $\Omega = \frac{2\pi}{24h}$; t = universal time; and n is an integer (= 1 is 'diurnal'; = 2 is 'semidiurnal'; = 3 is 'terdiurnal', etc.). The periodicity in longitude (λ) is given by the zonal wavenumber s, and the zonal phase speed (positive eastward) is given by $C_{ph} = -\frac{n\Omega}{s}$. $A_{n,s}$ and $\phi_{n,s}$ are the amplitude and phase, respectively, and are functions of height and latitude. We use the shorthand notation DWs or DEs to denote a westward or eastward propagating diurnal tide, respectively, with s in this case denoted by its absolute magnitude. For semidiurnal and terdiurnal oscillations, 'S' and 'T' replace 'D'. The zonally symmetric oscillations are denoted D0, S0, and T0. Stationary planetary waves with zonal wavenumber s are denoted SPWs.

The main sources for solar thermal tides appearing at 110 km in the Earth's atmosphere include latent heat release and infrared radiative absorption by H_2O in the troposphere (Forbes and Garrett 1978, 1979; Hagan and Forbes 2002, 2003; Zhang et al. 2010a, 2010b) and UV radiative absorption by O_3 in the stratosphere and lower mesosphere (Forbes and Garrett 1978). Some parts of the tidal spectrum remain trapped near the levels of excitation (Hagan and Roble 2001) while others belong to the class of waves that are vertically propagating. The vertically propagating part of the spectrum that reaches 100 to 130 km altitude maximizes there as molecular dissipation sets in (Forbes and Garrett 1979). At 110 km and equatorward of about 50°, the tidal fields that have propagated vertically from lower atmosphere sources dominate over those tides excited *in situ* from EUV solar radiation absorption (Forbes and Garrett 1979). From a climatological perspective, the dominant thermal excitation sources for nonmigrating tides reside in the troposphere, although during special events such as sudden stratosphere warmings ozone distributions can become sufficiently longitude dependent that non-negligible nonmigrating tides can possibly be excited (Goncharenko et al. 2012). Nonmigrating tides can also be excited by nonlinear tide-tide interactions, e.g., (Akmaev 2001; Du and Ward 2010; Hagan et al. 2009; Huang et al. 2007; Moudden and Forbes 2013; Smith and Ortland 2001), and interactions between tides and stationary planetary waves [e.g., (Coll and Forbes 2002; Chang et al. 2009; Forbes and Wu 2006; Lieberman et al. 2004; Liu et al. 2002; Yamashita et al. 2010)]; these sources of tides at 110 km are discussed in the 'Conclusions' section of this paper. For now, we proceed in the context of tropospheric excitation of nonmigrating tides.

Some insight into the nonmigrating tides that are produced by tropospheric heat sources and that are expected to enter the thermosphere at 110 km are provided in Figure 1, which was constructed based on data generated in the work of Zhang et al. 2010a, 2010b. These

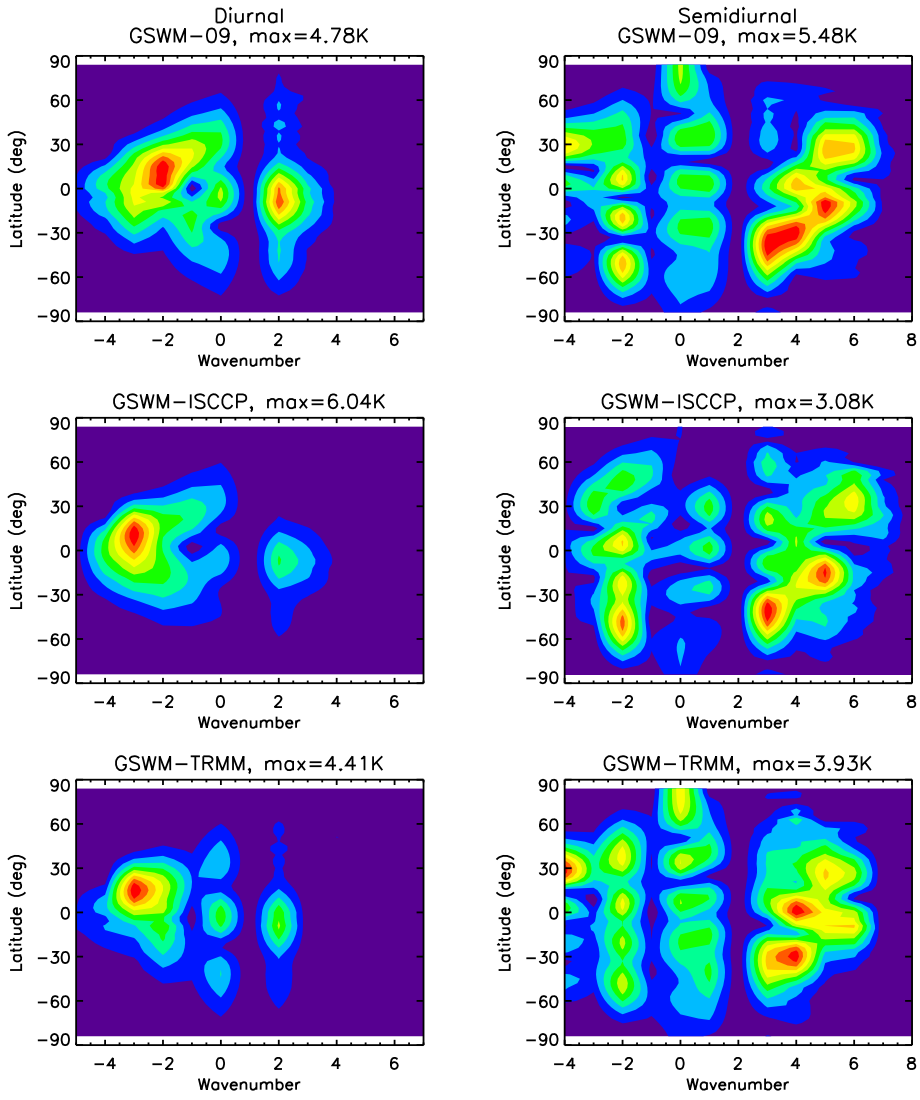

Figure 1 GSWM-09 simulations of nonmigrating diurnal (left) and semidiurnal (right) tidal temperature amplitudes. GSWM-09 simulations of nonmigrating diurnal (left) and semidiurnal (right) tidal temperature amplitudes at 110 km, based on the work of Zhang et al. 2010a, 2010b. Bottom: tropospheric latent heat forcing only, based on TRMM data products. Middle: tropospheric radiative heating only, based on ISCCP data products. Top: combined tropospheric latent and radiative heating. The dominant migrating components are excluded to better highlight the smaller nonmigrating components.

figures compare diurnal and semidiurnal nonmigrating tidal temperature spectra at 110 km from the following sources: Global Scale Wave Model (GSWM) calculations taking into account both radiative and latent heating in the troposphere based on International Satellite Cloud Climatology (ISCCP) reanalysis and Tropical Rainfall Measurement Mission (TRMM) measurements, respectively (top row); ISSCP-based radiative forcing only (middle row); and TRMM-based latent heat forcing only (bottom row). Results from November are illustrated to complement published figures for January and September; see Zhang et al. 2010a, 2010b for details. These results are generally representative of those tidal components that are (or are not) likely to be generated by tropospheric heating throughout the year. From Figure 1, we see that the nonmigrating diurnal (semidiurnal) tides that dominate the spectrum are D0, DW2, DE1, DE2, and DE3 (SW1, SW3, SW4, SW5, SW6, and SE2). We note also that the tides forced by radiative heating are comparable in magnitude to those generated by latent heating. No GSWM simulations are available for the terdiurnal tide, due to the limited time resolution of the ISCCP and TRMM data sets.

An important underlying reason why many of these wave components exist is due to the influence of land-sea and topographic differences [e.g., (Yagai 1989)] on the global distributions of latent heat release and water

vapor. As explained in Forbes et al. 2006 and earlier works (Tokioka and Yagai 1987; Hendon and Woodberry 1993; Williams and Avery 1996), to first order the longitudinal wavenumber $m = 4$ land-sea variation modulates the absorption of the diurnal (westward-propagating 24-h harmonic) of solar radiation (and subsequent convection and latent heat release) to produce DE3 and DW5, whereas $m = 1$ produces D0 and DW2. These $m = 4$ and $m = 1$ zonal surface variations similarly modulate the semidiurnal and terdiurnal heating distributions to force the following waves, respectively: SW6, SE2, SW1, SW3, TW7, TE1, TW4, and TW2.

There are of course other Fourier components of land-sea difference that generate still more pairs of diurnal, semidiurnal, and terdiurnal tides (Zhang et al. 2010b). The degree to which any of these wave components reach 110 km depends on the relative efficiencies with which they are generated but also on their sensitivity to background atmospheric conditions between the troposphere and 110 km. For instance, DW5 has a very short vertical wavelength and is therefore relatively more susceptible to dissipation; in addition, due to its large zonal wavenumber (and therefore slow zonal phase speed), DW5 may also be significantly influenced by the mean wind field.

We also know from classical tidal theory that very long vertical wavelength waves can undergo evanescent behavior in the mesosphere where the lapse rate is negative, thus temporarily limiting exponential growth of such waves. The term 'mesospheric barrier' is sometimes used in this context (Geller 1970). The atmosphere between the troposphere and lower thermosphere thus serves as a natural filter to the wave spectrum, removing both very short (ca. $<$25 km) and very long (ca. $>$200 km) waves. Throughout this paper, we will refer to vertical wavelengths in a very approximate sense, based on the simple formula:

$$\lambda_z \approx \frac{2\pi H}{\sqrt{\frac{H}{h_n}\kappa - \frac{1}{4}}} \tag{2}$$

where H is the atmospheric scale height for a 260 K isothermal atmosphere; h_n is the equivalent depth, related to the eigenvalue of a particular Hough function in classical tidal theory (Chapman and Lindzen 1970); and $\kappa = \frac{\gamma-1}{\gamma}$ where γ is the ratio of specific heats $\frac{c_p}{c_v}$. A slightly better approximation exists that includes the gradient of temperature (and thus leads to the notion of a mesospheric barrier noted above), but even in this case, the formula is not applicable where the temperature varies too much with height. For our purposes, we will speak about vertical wavelength in very general and relative terms, and the simple approximation above is adequate. For reference, vertical wavelengths obtained from the above formula are tabulated in Table 1.

Table 1 Diurnal and semidiurnal vertical wavelengths (km) from classical tidal theory based on a T = 260 km isothermal atmosphere

s	D1S	S1S	D1A	S1A	D2S	S2S	D2A	S2A
-3	56	-	30	91	*	56	*	44
-2	108	-	38	183	*	77	*	52
-1	-	-	53	-	*	118	*	65
0	27	-	102	-	*	87	*	56
1	28	-	*	128	*	67	*	48
2	27	-	*	82	*	54	*	41
3	25	105	*	62	*	45	*	36
4	*	72	*	50	*	39	*	32
5	*	56	*	43	*	35	*	29
6	*	46	*	37	*	31	*	27

D1S, diurnal 1st symmetric; S1S, semidiurnal 1st symmetric; D1A, diurnal 1st antisymmetric and so on; *, $<$25 km; -, $>$200 km.

It is not uncommon for comprehensive numerical models or observational data in the mesosphere and lower thermosphere to reflect the presence of tidal structures that appear very similar to the Hough functions of classical tidal theory. Even the distorting effects of mean winds tend to result in linearly independent tidal modes that individually have the characteristics of Hough modes of tidal theory (Lindzen and Hong 1974; Walterscheid and Venkateswaran 1979a; 1979b). This will often be the case in the present paper as well. For later reference, Hough functions for many of the key tidal responses studied in the present paper are illustrated in Figure 2. These correspond to the vertically propagating class of tidal modes and include the first symmetric and first antisymmetric structures of D0, DE1, DE2, and DE3 and the first symmetric structures of DW1, DW2 and DW3. Generally, vertical wavelengths decrease as the magnitudes of zonal wave numbers increase, and eastward-propagating waves of a given wavenumber have longer vertical wavelengths than their westward-propagating counterpart. Also, the first symmetric or antisymmetric mode has a longer vertical wavelength than the second symmetric or antisymmetric modes, and so on. This is why only the first symmetric modes of DW1, DW2, and DW3 are shown in Figure 2; while these waves have vertical wavelengths (approximately 25 to 30 km) that allow them access to 110 km (albeit not very efficiently), the antisymmetric components of DW1, DW2, and DW3 have even shorter vertical wavelengths and are not seen in observations at 110 km.

Also shown in Figure 2 are the first symmetric and antisymmetric components of the vertically propagating SE1, SE2, SE3, SW2, SW4, and SW6 (structures of SW1, SW3, and SW5 are very similar to those shown for SW2, SW4, and SW6). The similarities in horizontal structure

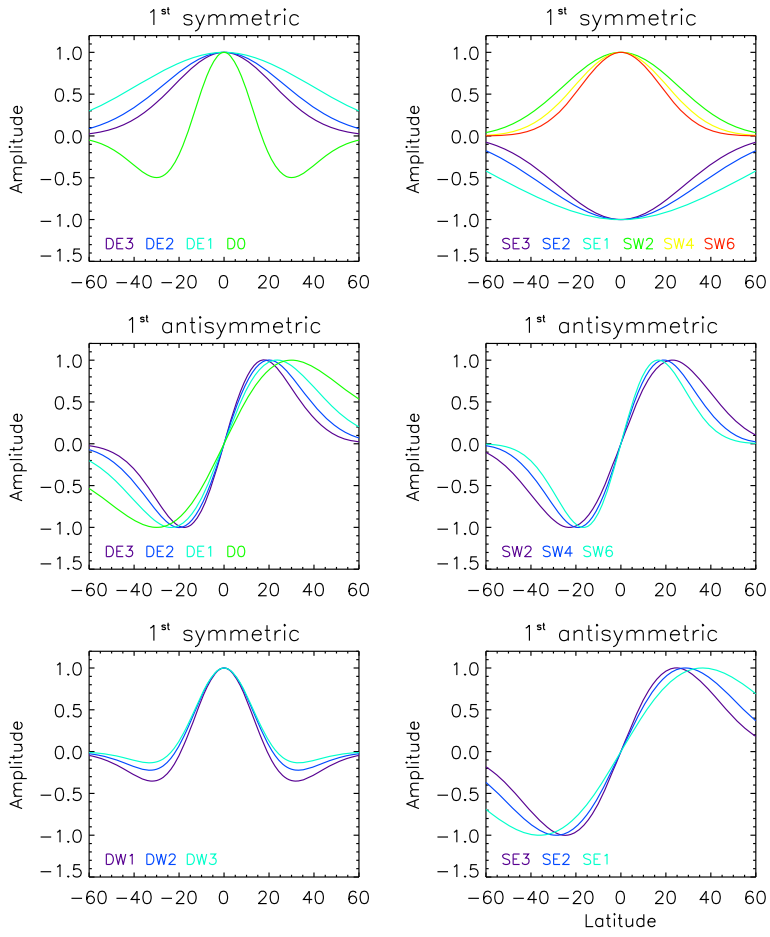

Figure 2 First symmetric and first antisymmetric Hough functions. First symmetric and first antisymmetric Hough functions for the diurnal and semidiurnal tidal components considered in this study.

between all of these waves are obvious. However, the first symmetric eastward-propagating waves have very long vertical wavelengths and are significantly attenuated by the mesospheric barrier. The same is true for the first symmetric components of S0, SW1, and SW2. This leaves open the possibility that many of the semidiurnal structures will be antisymmetric or very asymmetric in character, contrary to the diurnal part of the spectrum. This is indeed what we will find.

In this paper, it is our goal to present the seasonal-latitudinal structures of all the wave components of importance at 110 km. Many of these are presented for the first time. A second goal is to interpret the presence of these waves and their structures based on the information given above in connection with Figures 1 and 2. The data and methodologies employed in our study to achieve these goals are briefly reviewed in the 'Data and tidal analysis method' section. The 'Results and discussion' and 'Conclusions' sections present our results and conclusions, respectively.

Data and tidal analysis method

The data employed in this study are TIMED/SABER Version 07 temperature measurements extending from 2002 through 2010. The tidal fields are displayed at 110 km (in a few cases 100 km) since this is the highest altitude where high confidence exists in the temperature measurements and where most of the waves achieve their highest amplitudes within the SABER data set. Moreover, 110 km lies within the ionospheric dynamo region, and knowledge of the tidal spectrum there has important implications for ionosphere, as described in the 'Background' section. The data are processed in a manner identical to that detailed in Forbes et al. 2008 and a full description of this methodology is not repeated here. Basically, 60-day mean tidal amplitudes are obtained on the 15th of each month by binning residuals from a running 60-day mean in local time and longitude and fitting these residuals with the cosine and sine terms equivalent to Equation 1 to obtain amplitudes and phases of the various tidal components. A noise floor is defined to establish a detectability

limit for components of the tidal spectrum. Due to yaw cycle maneuvers, data are only continuously available between ±50° latitude, and our tidal analyses are limited accordingly.

Results and discussion

Tidal spectra

Spectra for the diurnal, semidiurnal, and terdiurnal solar tides are depicted in Figures 3, 4, and 5, respectively. Migrating tides (DW1, SW2, TW3) are omitted from these figures to better highlight the generally smaller nonmigrating components. Each figure shows wave numbers in the range ±6 about the migrating tide values of 1, 2, and 3 for DW1, SW2, and TW3, respectively. The top, middle, and bottom rows of each figure correspond to −25°, 0°, and +25° latitude, respectively. The seasonal-latitudinal structures of the important tidal components will be illustrated in forthcoming Figures 6, 7, 8, 9, and 10. Here our main purpose is to identify the main components and to comment on their potential origins in the context of Figure 1.

In the diurnal tide spectra in Figure 3, DE3 is the prominent component followed in importance by DE2, DW2, and D0 and then DW3 and DW5. The presence of DE3, DE2, DW2, and D0 is consistent with expectations based on current estimates of tropospheric thermal excitation. However, this is not true for DW3 and DW5. Moreover, DW3 and DW5 have vertical wavelengths on the order of 25 km or less and thus are not expected to effectively propagate from the troposphere to 110 km. We must tentatively conclude, therefore, that these waves

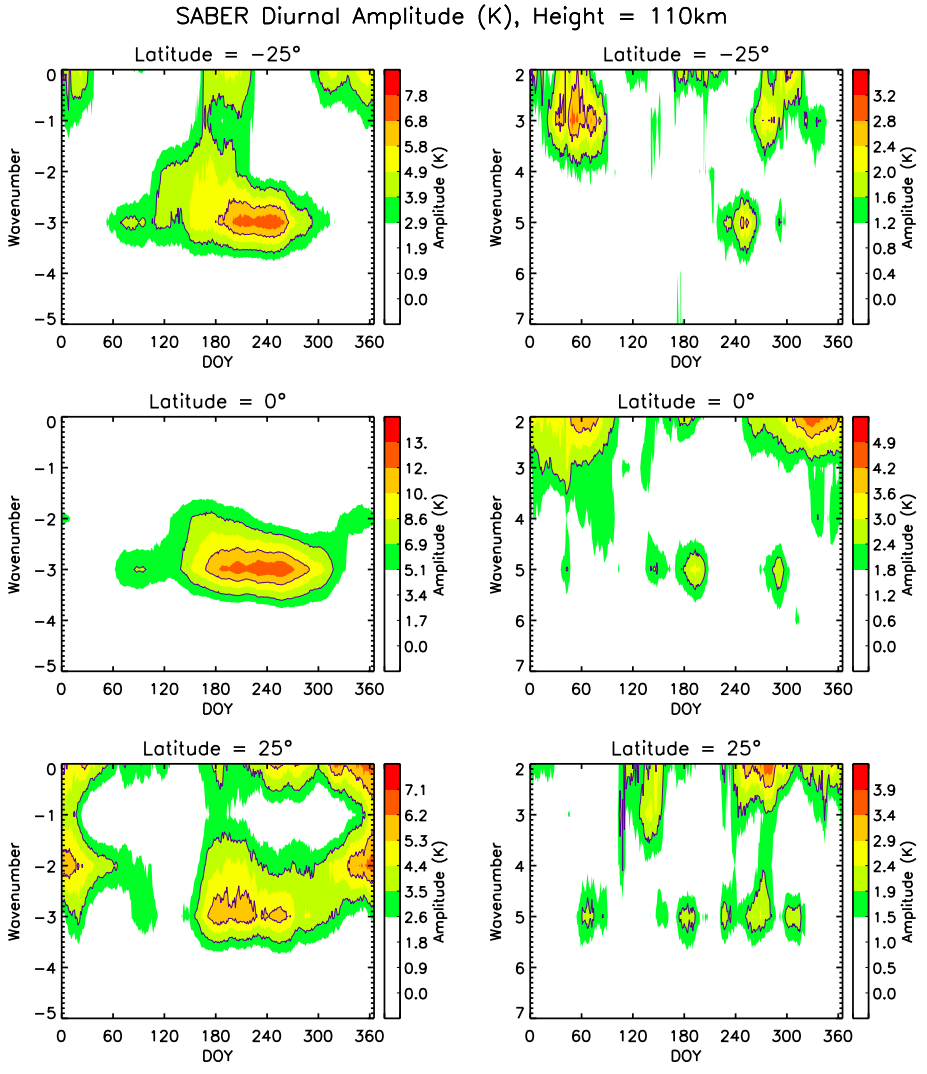

Figure 3 Wavenumber vs. day of year SABER diurnal nonmigrating temperature amplitude spectra. Wavenumber vs. day of year SABER diurnal nonmigrating temperature amplitude spectra at +25° (bottom), 0° (middle), and −25° (top) latitude.

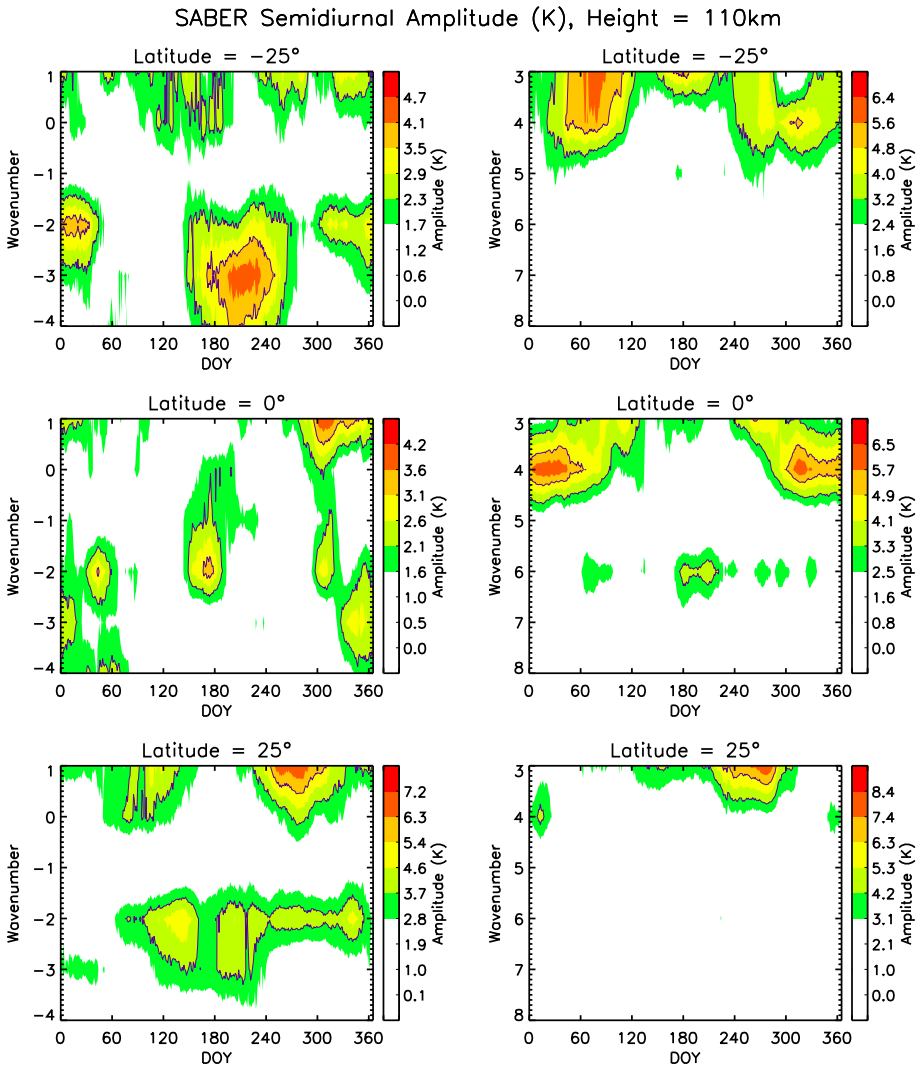

Figure 4 Same as Figure 3, except for semidiurnal tidal components.

may be excited *in situ* by nonlinear wave-wave interactions. The possible interactions are explored below in the 'Conclusions' section.

Figure 4 illustrates spectra for the semidiurnal tide. The largest components at the shown latitudes are SW4, SW3, and SW1 followed by SE3 and SE2. There are also occasional appearances of SE1, SE4, and SW6 at smaller amplitudes. Based on the results in Figure 1, SE4, SE2, SW1, SW3, SW4, SW5, and SW6 are expected to propagate upward from tropospheric heat sources, but SE1 and SE3 are not. Again, SE1 and SE3 may be excited *in situ*, and this possibility will be explored later in this paper, along with possible *in situ* origins of SE2, SW1, and SW3.

The most prominent terdiurnal tides illustrated in Figure 5 are TE1, TW7, and TW5. There are also lesser signatures of TW1, TW4, and TW2. There are no troposphere heating rates and related calculations (cf. Figure 1) for the terdiurnal tide, but as noted previously, TE1, TW7, TW2, and TW4 are consistent with the same arguments involving $s = 4$ and $s = 1$ components of land-sea difference offered as explanations for the existence of DE3, DW5, D0, DW2, SE2, SW6, SW1, and SW3. Moudden and Forbes 2013 studied the climatology of the terdiurnal tide using a higher-resolution method and found the largest and most repeatable components in this atmospheric region from year to year to be TE1, TW4, and TW5. Aliasing considerations precluded them from claiming reliable results for TW1 and TW2. These authors also put forth arguments that TE1, TW4, and TW5 arise as a result of nonlinear interactions between nonmigrating diurnal and semidiurnal tides. These possibilities are discussed further in the 'Conclusions' section.

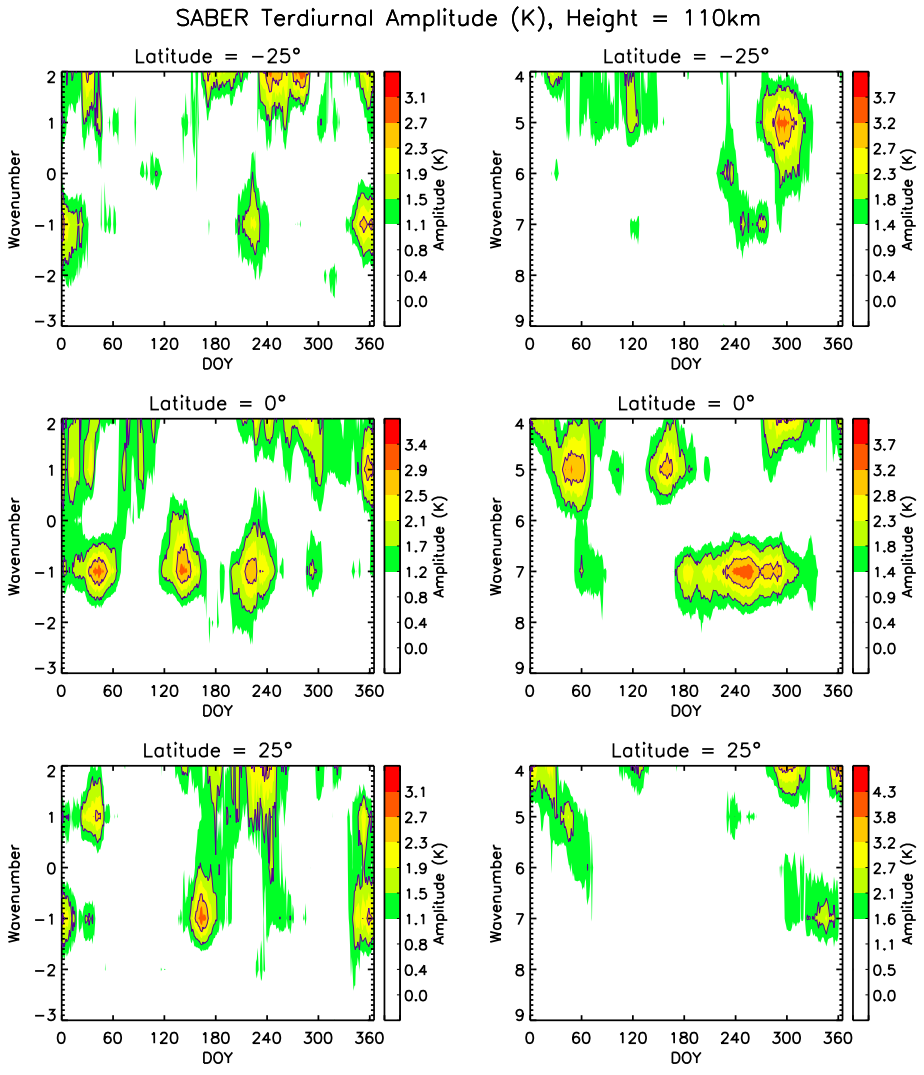

Figure 5 Same as Figure 3, except for terdiurnal tidal components.

The spectra in Figures 3, 4, and 5 provide a broad overview of the tidal components that are present and begin to provide some insight into possible origins of the waves. They also serve as guidance on what seasonal-latitudinal structures should be investigated further, and these are presented in the next subsection.

Seasonal-latitudinal structures

In Figures 6, 7, 8, 9, and 10, we present temperature amplitudes of the various tidal components discussed previously, in a latitude vs. day of year (DOY) format, vector averaged over 2002 to 2010 and extending between ±50° latitude at a height of 110 km. Additional files accompanying this manuscript are provided with the corresponding phases (universal time of maximum in hours at 0° longitude) in the same format as Figures 6, 7, 8, 9, 10, and 11. The corresponding file names for the phases are 'Additional file 1: Phases for Figure 6', 'Additional file 2: Phases for Figure 7', and so on. In viewing the phase structures in Additional files 1, 2, 3, 4, 5, and 6, the reader is cautioned to trust phases only in those regimes where the amplitudes exceed 1 to 2 K in Figures 6, 7, 8, 9, 10, and 11 in the main text. In addition, Table 2 contains a compilation of the likely origins of the waves (lower atmosphere heating and nonlinear wave-wave interactions) and the predominant Hough mode composition of the most well-defined seasonal-latitudinal structures at 110 km.

We begin with the seasonal-latitudinal structures of the migrating diurnal (DW1), semidiurnal (SW2), and terdiurnal (TW3) tides in Figure 6. Examination of vertical structures of these tidal components (not shown in this paper) reveals that significant signatures of the *in situ*-driven migrating tides do not appear until about 115 to 120 km; thus the migrating tides shown here originate in

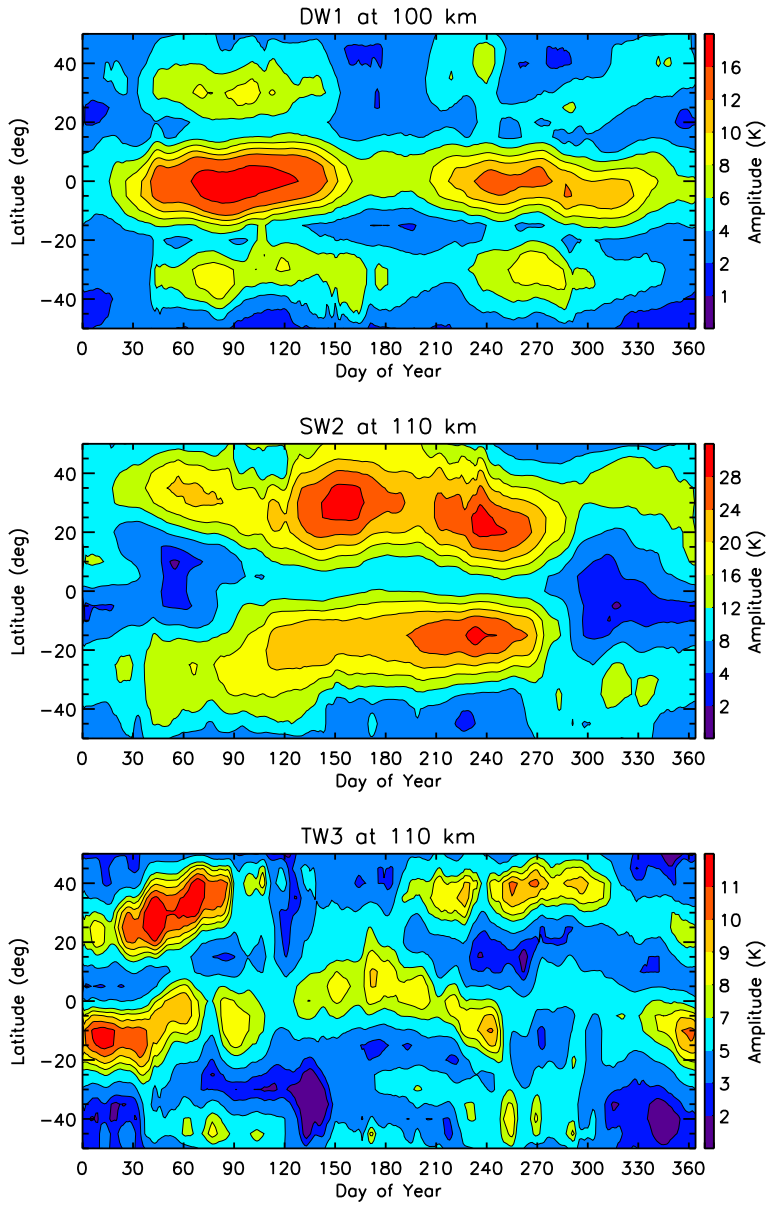

Figure 6 Latitude vs. day of year variation of SABER temperature amplitudes. Latitude vs. day of year variation of SABER temperature amplitudes for migrating tidal components DW1 (top), SW2 (middle), and TW3 (bottom).

the lower atmosphere. Since DW1 reaches its peak amplitude near 100 km in the SABER temperature data, this is the altitude shown for DW1 in this figure. DW1 exhibits amplitude maxima at the equator during February to April and August to October and secondary maxima at about ±20°−40° latitude. This type of latitude structure is consistent with the first symmetric Hough function for DW1 plotted in Figure 2. The approximately 12-h shift in phase between the equator and ±20°−40° latitude in 'Additional file 1: Phases for Figure 6' support this interpretation. While other Hough mode components are excited in the lower atmosphere, they are either trapped there due to their evanescent vertical structure or propagate with very short wavelengths and thus dissipated before reaching 100 km.

SW2 shown in the middle panel of Figure 6 is more antisymmetric in nature, with minima occurring near the equator, and largest amplitudes occurring during February to September. There are two reasons for this asymmetric behavior. First, the first symmetric mode of SW2, which actually accounts for a significant fraction of the forcing, has a very long vertical wavelength, and its exponential growth is curtailed within the mesospheric barrier. In addition, the interaction of this symmetric

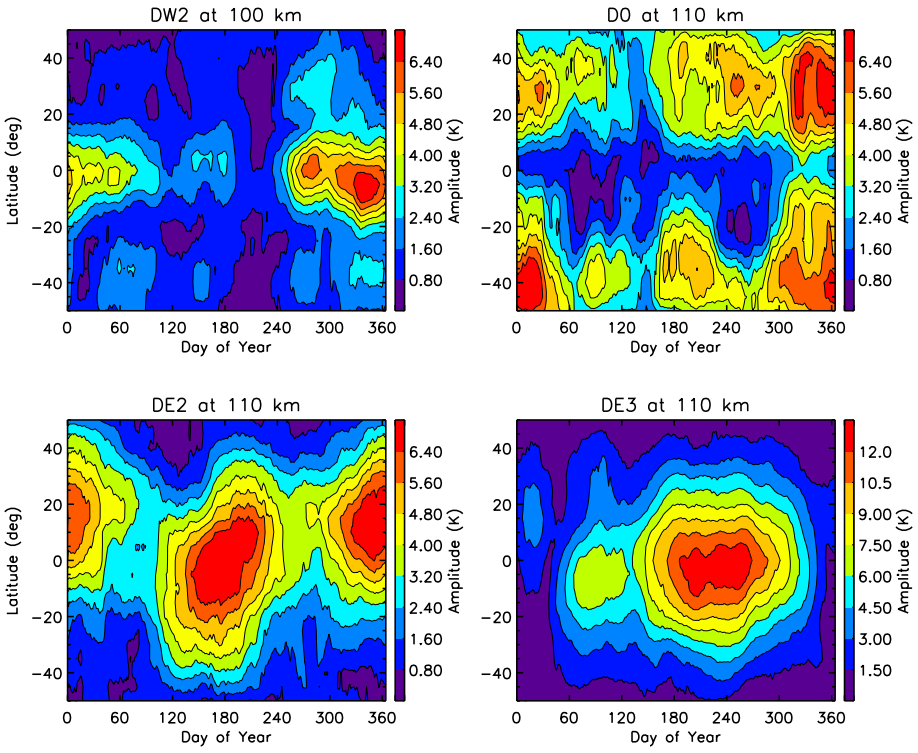

Figure 7 Latitude vs. month depictions of multi-year average SABER temperature amplitudes. Latitude vs. month depictions of multi-year average SABER temperature amplitudes for DW2 at 100 km, and D0, DE2, and DE3 at 110 km.

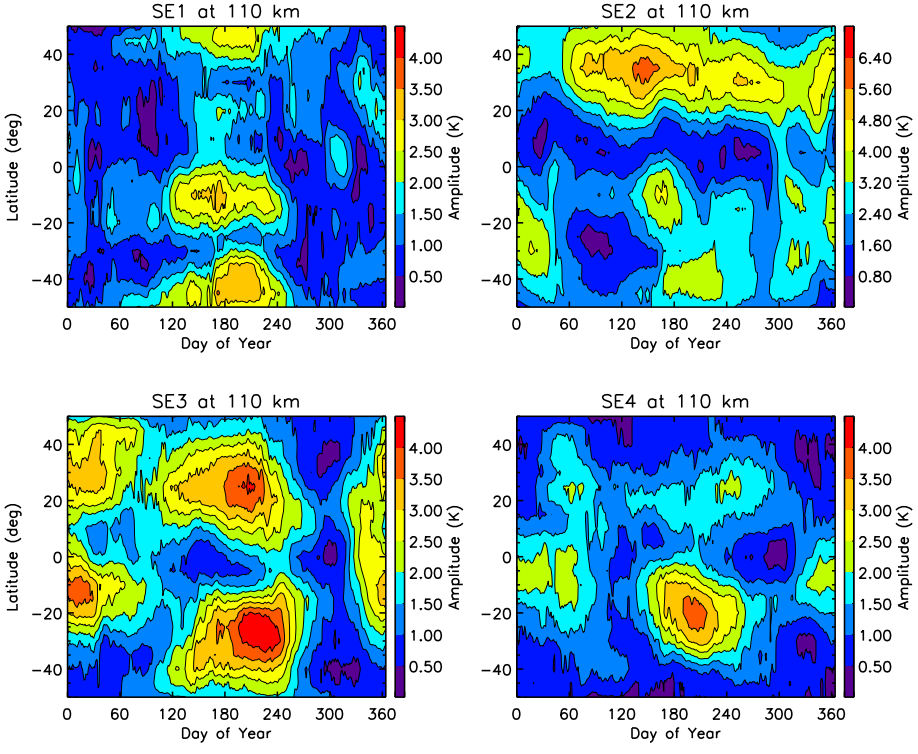

Figure 8 Latitude vs. month depictions of multi-year average SABER temperature amplitudes. Latitude vs. month depictions of multi-year average SABER temperature amplitudes for SE1, SE2, SE3, and SE4 at 110 km.

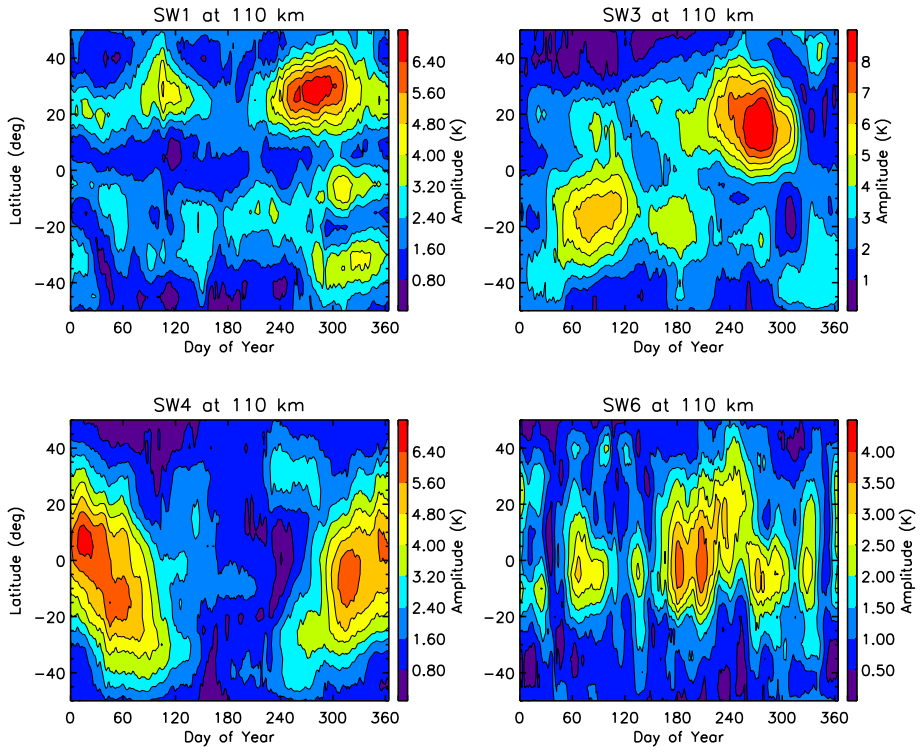

Figure 9 Latitude vs. month depictions of multi-year average SABER temperature amplitudes. Latitude vs. month depictions of multi-year average SABER temperature amplitudes for SW1, SW3, SW4, and SW6 at 110 km.

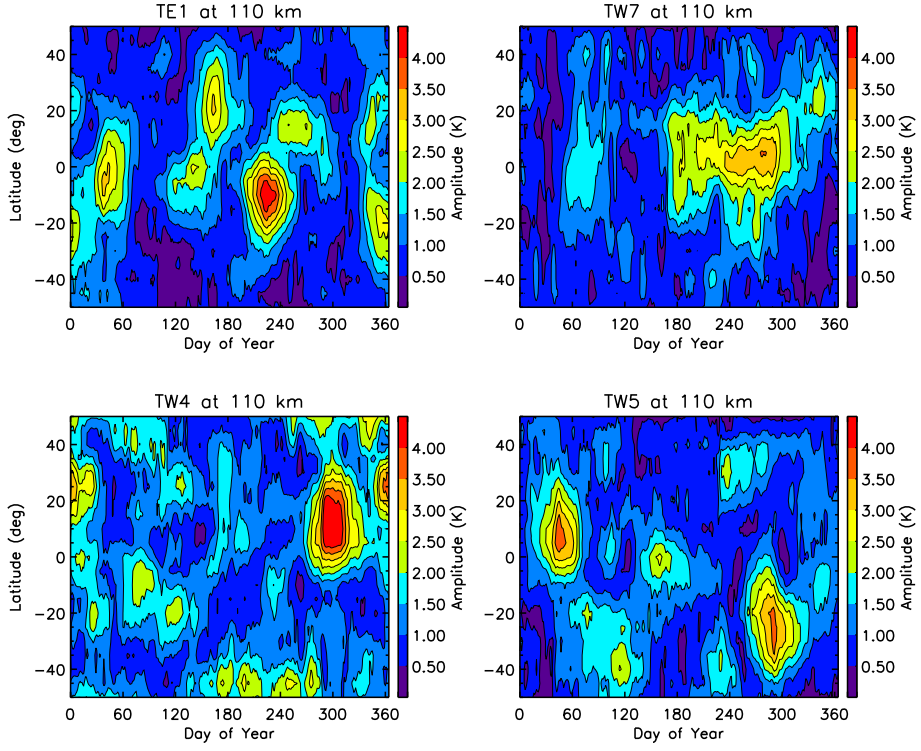

Figure 10 Latitude vs. month depictions of multi-year average SABER temperature amplitudes. Latitude vs. month depictions of multi-year average SABER temperature amplitudes for TE1, TW7, TW4, and TW5 at 110 km.

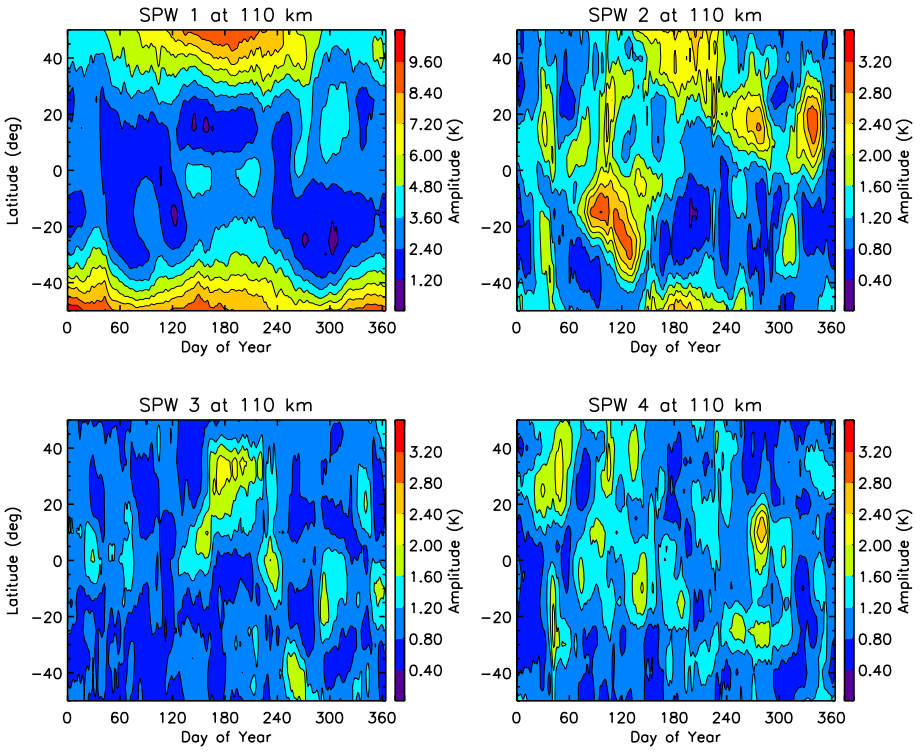

Figure 11 Latitude vs. month depictions of multi-year average SABER temperature amplitudes. Latitude vs. month depictions of multi-year average SABER temperature amplitudes for stationary planetary wave components SPW1, SPW2, SPW3, and SPW4 at 110 km.

Table 2 Likely origins and predominant Hough mode compositions of well-defined solar thermal tidal components at 110 km as illustrated in Figures 6, 7, 8, 9, and 10

Tidal component	Excited by lower atmosphere heating	Excited by nonlinear wave-wave interactions	First symmetric mode relative importance	First antisymmetric mode relative importance	Higher-order modes relative importance
DW1	*		1	0	0
SW2	*		2	1	3
TW3	*	*	3	1	2
DE3	*		1	2	0
DE2	*		1	2	0
D0	*	*	0	1	2
DW2	*	*	1	0	0
SE1		*	0	2	1
SE2	*	*	0	2	1
SE3		*	0	1	2
SE4	*		0	1	2
SW1	*	*	0	2	1
SW3	*	*	1	1	2
SW4	*		1	1	2
SW6	*		1	2	0
TW7	*		1	2	0

*, indicate in the affirmative whether the indicated tidal component is likely excited by lower atmosphere forcing and/or nonlinear wave-wave interactions.

mode with the largely non-symmetric middle atmosphere zonal wind jets 'couples' into the first antisymmetric mode to accommodate this distortion in the total semidiurnal tidal structure. This first antisymmetric mode freely propagates with height and maximizes in the approximately 110-km region. The significant differences in phase between the $\pm 10°-40°$ latitude bands between the N. and S. hemispheres clearly indicates the presence of a strong antisymmetric component (see 'Additional file 1: Phases for Figure 6'). However, note from Figure 2 that the first antisymmetric mode of SW2 peaks close to $\pm 20°$ latitude, whereas the structures in Figure 6 often peak close to $\pm 30°$ latitude. This means that higher-order Hough components of SW2 are probably embedded in these structures and that there are additional, probably secondary, maxima occurring at latitudes poleward of $\pm 50°$ latitude.

The terdiurnal migrating tide TW3 is displayed in the bottom panel of Figure 6. A comprehensive study of the terdiurnal tide in SABER data has recently been published by Moudden and Forbes 2013, and the reader is referred there for details on prior works and theories. Current theories (Akmaev 2001; Huang et al. 2007; Smith and Ortland 2001) appear to be in agreement that some part of TW3 is forced thermally, while an important contribution also arises through nonlinear interaction between DW1 and SW2. We also note that TW3 at 110 km can be comparable to or greater than either SW2 or DW1 at certain latitudes and days of the year. Furthermore, its banded structure and sometimes occurrence of triple peaks in latitude suggest that at least four and perhaps up to six Hough components of TW3 would be required to capture the structures seen in Figures 6.

Figure 7 displays the seasonal-latitudinal structures of DW2, D0, DE2, and DE3. All of these waves have thermal sources in the troposphere (cf. Figure 1). Similar to DW1 and for the same reasons noted above, DW2 displays a mainly symmetric structure about the equator. The approximately 12-h shift in phase between the $\pm 20°$ latitude band and middle latitudes supports this interpretation (see 'Additional file 2: Phases for Figure 7'). On the other hand, D0 has minimum amplitudes near the equator, and its latitude structure is similar to that of the first antisymmetric mode of D0 plotted in Figure 2. As shown in 'Additional file 2: Phases for Figure 7', D0 is nearly in anti-phase between the N. and S. hemispheres and, moreover, does not change much throughout the year. Similar to SW2, the first symmetric mode of D0 is evanescent in the mesospheric barrier and may additionally be less efficiently forced in the troposphere than the antisymmetric component.

The seasonal-latitudinal structures of DE2 and DE3 are shown in the bottom panels of Figure 7. The first symmetric mode of DE3 is of order 50 to 60 km, whereas that of DE2 is greater than 100 km (see Table 1). The symmetric structure of DE3 can therefore be understood by the fact that its first symmetric component freely propagates vertically, whereas its first antisymmetric component has a vertical wavelength of order 30 km and does not effectively propagate to 110 km. On the other hand, the first symmetric component of DE2 is likely diminished in the mesospheric barrier, whereas its first antisymmetric component, with vertical wavelength near 40 km, more easily propagates to 110 km. This likely accounts for the difference in symmetry between DE3 and DE2, but of course, the relative efficiencies with which the various Hough components are generated in the troposphere also play a role as well. The greater presence of an antisymmetric component in DE2 is consistent with the approximately 3-h phase shift between hemispheres shown in 'Additional file 2: Phases for Figure 7', whereas the phases for DE3 (when amplitudes are significant) are symmetric about the equator.

Figure 8 displays the seasonal-latitudinal structures of SE1, SE2, SE3, and SE4. Since the first symmetric modes of all of these oscillations possess very large vertical wavelengths, the mesospheric barrier precludes their prominence in these structures, and this is even true for the first antisymmetric components of SE1 and SE2. This partially explains why SE3 and SE4 are more similar to their first antisymmetric Hough modes in Figure 2, whereas the latitudinal structures of SE1 and SE2 are more complex and likely contain relatively large contributions from higher-order Hough modes. For instance, the phase structure for SE1 in 'Additional file 3: Phases for Figure 8' indicates strong presence of the second symmetric mode between days 120 and 240, whereas an antisymmetric phase structure (approximately 5- to 7-h phase difference between hemispheres) is evident during much of the year for SE3 and SE4. SE2 is a little more complicated, indicating a greater degree of mixed symmetric and antisymmetric components. Another noteworthy aspect of these semidiurnal components is that while SE2 and SE4 result from troposphere heating, SE1 and SE3 do not, to any significant degree. This suggests a different origin might be possible for SE1 and SE3, which is discussed further in the following section.

Seasonal-latitudinal structures for SW1, SW3, SW4, and SW6 are presented in Figure 9. Comparison with Figure 1 indicates that all of these waves have the potential to be excited by tropospheric heat sources. The first two modes of SW1 have long vertical wavelengths and are likely impeded by the mesospheric barrier; the structures seen here likely contain significant contributions from the second symmetric and antisymmetric components, and perhaps even higher modes. As one progresses from SW3 to SW4 to SW6, the higher-order modes have progressively shorter vertical wavelengths (several of them <30 km), which explains the greater dominance of the first

symmetric mode in this progression. For instance, the SW3 and SW4 latitudinal structures in Figure 9 can easily be approximated by the sum of the first symmetric and antisymmetric waves in Figure 2, whereas SW6 consists primarily of the first symmetric mode with maximum at the equator. The phase structures in 'Additional file 4: Phases for Figure 9' confirm this progression; SW3 indicates the presence of lower-order modes than SW1, and the symmetry vs. antisymmetry of the phases for SW4 follow those of the amplitude structures in Figure 9 and are furthermore simpler than the phase structures for SW3. Although the phases for SW6 vary with DOY, they generally indicate symmetry about the equator within the $\pm 20^\circ$ latitude band, in line with the equatorially confined amplitudes in Figure 9.

Figure 10 presents results for the terdiurnal components that survived vector averaging over the 9 years from 2002 to 2010. These waves achieve amplitudes of up to 4 K and are comparable to the amplitudes of SE1 to SE4 and SW6. As noted previously, estimates of tropospheric forcing for terdiurnal tides are not available, due to the coarse time resolution of available data. Furthermore, the existence of the TE1 and TW7 pair would be consistent with the same wave-4 modulation process that accounts for the excitation of DE3, DW5, SE2, and SW6. TW7 is thus analogous to SW6 in form and possible origin. TE1 is similar in many ways to SE1 in that many of its Hough components have long vertical wavelengths and that the surviving modes likely result in considerable latitudinal structure. However, there is a strong possibility that TE1 is excited by nonlinear interactions higher in the atmosphere, which mutes these types of arguments. The same is true for TW4 and TW5, which are discussed further in the following section. Concerning the phase structures in 'Additional file 5: Phases for Figure 10', if one focuses on the periods where the amplitudes exceed 2 K in Figure 10, the phase structures for TE1 and TW7 are coherent and indicate the degree of asymmetry or asymmetry expected in accord with the amplitude structures in Figure 10. This is somewhat remarkable given that the displayed amplitude and phase structures emerged from 60-day vector averages for the period 2002 to 2010 and thus may favor the argument that they arise from a single coherent tropospheric source.

Conclusions

In this paper, we quantify the climatological tidal spectrum entering the IT system at 110 km; identify the existence of the following waves: DE3, DE2, D0, DW1 to DW3, DW5, SE1 to SE4, S0, SW1 to SW4, SW6, TE1, TW1 to TW5, and TW7; and depict seasonal-altitudinal structures between $\pm 50^\circ$ latitude for most of them. For the subset of waves that have the most well-defined seasonal-latitudinal structures in Figure 6, 7, 8, 9, and 10, Table 2 contains a compilation of the likely origins of the waves and the predominant Hough mode content for each of them. The displayed temperature amplitudes represent vector averages covering 2002 to 2010 and thus likely underestimate actual amplitudes during some years. These waves all have accompanying wind fields that drive dynamo electric fields, which in turn impose considerable structure on the overlying F-region ionosphere. Some of these waves propagate to much higher levels in the thermosphere and drive variability in the neutral atmosphere, which in turn affects the ionosphere in additional ways. Part 2 of this 2-part study investigates vertical penetration of the tidal spectrum to the upper thermosphere.

Attribution of the tidal spectrum at 110 km to specific sources and propagation conditions at lower altitudes is a difficult problem that remains to be solved. In this paper, we noted that some waves could potentially be excited by lower atmosphere heating, based on recent estimates of radiative and latent heating sources. However, this does not preclude the existence of other sources for these waves, such as wave-wave interactions. In addition, our connection with tropospheric sources, at least in this paper, has been mostly qualitative. In future works, we will make more quantitative connections between wave sources and the atmospheric responses. Nevertheless, at this point, we would like to offer some suggestions as to what waves are likely to be generated by nonlinear interactions (see summary of following in Table 2). To augment this discussion, we have also examined height vs. latitude amplitude and phase structures (not shown) of all the waves discussed in this paper and have made assessments as to which waves have clear extensions down to approximately 70 km altitude with phase progression characteristics that indicate upward propagation.

To assess nonlinear interactions as a potential source for the tides that we delineate in this paper, we first refer to the seminal work of Teitelbaum and Vial 1991. Based on this work, it is now generally accepted, with many examples in observational data and in models, that the nonlinear interaction between two primary waves of frequency σ_1 and σ_2 and zonal wave numbers s_1 and s_2 yields secondary waves with the 'sum and difference' frequencies and zonal wavenumbers: $(\sigma_1 + \sigma_2, s_1 + s_2)$ and $(\sigma_1 - \sigma_2, s_1 - s_2)$:

$$\begin{aligned} &\cos(\sigma_1 t + s_1\lambda) \cdot \cos(\sigma_2 t + s_2\lambda) \rightarrow \\ &\cos[(\sigma_1 + \sigma_2)\, t + (s_1 + s_2)\, \lambda] + \cos[(\sigma_1 - \sigma_2)\, t \\ &\quad + (s_1 - s_2)\, \lambda] \end{aligned} \tag{3}$$

Moreover, to first order these, secondary waves propagate vertically and horizontally as independent waves. According to this theory, self interactions are inefficient. While there remain many questions to be addressed, such as what the optimum conditions are and relative efficiencies under which each secondary wave is produced,

we will proceed on the grounds that the theory can at least qualitatively predict the possible presence of certain waves.

Several well-established examples of secondary-wave production occur through the interaction between traveling planetary waves and tides, e.g., (Beard et al. 1999; Kamalabadi et al. 1997; Pancheva and Mitchell 2004); however, these interactions produce secondary waves at non-tidal periods. Wave-wave interactions that produce waves at tidal periods include tide-tide interactions and interactions between tides and stationary planetary waves. One example of a tide-tide interaction relevant to the present study was revealed in the ionosphere-thermosphere general circulation simulations of Hagan et al. 2009. They demonstrate that the interaction between DW1 and DE3 in the model yield secondary waves SE2 and SPW4 of substantial magnitude in the lower thermosphere. In the following, we will use the following shorthand notation to describe such interactions, where the secondary waves are given in the order 'sum', 'difference': $DW1 \cdot DE3 \rightarrow SE2, SPW4$.

The migrating terdiurnal tide is perhaps the earliest example wherein a nonlinear tide-tide interaction was invoked to explain its origin. Various numerical models provide evidence that $DW1 \cdot SW2 \rightarrow TW3, DW1$ contributes to the excitation of TW3, but are in disagreement regarding the relative importance of this source and thermal excitation (Akmaev 2001; Du and Ward 2010; Huang et al. 2007; Smith and Ortland 2001). Recent studies of the terdiurnal tide have also focused on nonmigrating components (Du and Ward 2010; Moudden and Forbes 2013; Yue et al. 2013).

Concerning the interaction between tides and stationary planetary waves, the interaction $SW2 \cdot SPW1 \rightarrow SW1, SW3$ is one that is now well accepted as being operative in the atmosphere from both observational and modeling points of view [e.g., (Coll and Forbes 2002; Chang et al. 2009; Forbes and Wu 2006; Lieberman et al. 2004; Liu et al. 2010; Yamashita et al. 2002)], particularly so during sudden stratosphere warmings (SSW) with consequences for ionospheric variability [(Chau et al. 2009; Goncharenko and Zhang 2008; Liu and Roble 2002; Liu et al. 2010; Pedatella and Forbes 2010; Sridharan et al. 2009)]. By the same reasoning, interaction between SPW1 and DW1 could give rise to DW2 and D0, and migrating tide interactions with SPW2 could give rise to S0, SW4 and DE1, DW3. Considering these and other potential possibilities, the seasonal-latitudinal structures of SPW1, SPW2, SPW3, and SPW4 at 110 km are shown in Figure 11 and the corresponding phases are in 'Additional file 6: Phases for Figure 11'. We note that SPW1 and SPW2 are the only stationary wave components at this level that have amplitudes comparable to many of the tidal components that we are seeking to explain. The signatures of SPW1 likely reflect the upward extension of SPW1 from lower altitudes and latitudes, as well as possibly some influence of high-latitude processes and displaced geomagnetic and geographic coordinate systems. It is noteworthy that a coherent pattern for SPW4 does not appear in this figure, although one would be expected based on the modeling work of (Hagan et al. 2009). It is possible that inter-annual variability in phase has caused such a signature to be washed out in a multi-year vector average or that the SPW4 wave achieves more appreciable amplitudes at higher altitudes.

With the above as background, we now summarize what we can conclude concerning attribution of the various waves revealed in this study (see also summary in Table 2). For the diurnal tides, DE3, DE2, D0, DW1, and DW2 possess strong signatures of upward propagation from lower atmosphere sources and can be considered 'primary' waves in discussions involving wave-wave interactions. For D0 and DW2, it is possible that $DW1 \cdot SPW1 \rightarrow DW2, D0$ augments tropospheric heating as a source. However, as mentioned previously, DW3 and DW5 must be excited *in situ* in the lower thermosphere. Viable candidates appear to be $DW2 \cdot SPW1 \rightarrow DW3, DW1$ and $DE3 \cdot SW2 \rightarrow TE1, DW5$.

The latter interaction between DE3 and SW2 also serves as an *in situ* source for TE1 and in fact reinforces the contention by Moudden and Forbes 2013 that this interaction serves as an important source for TE1 throughout the atmosphere. As noted earlier in this paper, another logical source for TE1 arises as a result of wave-4 modulation of the terdiurnal component of radiative and latent heating in the troposphere, which is also a viable candidate for production of TW7 seen in Figure 10. They also provide evidence that the following interactions are responsible for the generation of TW4 and TW5: $DW2 \cdot SW2 \rightarrow TW4, D0$, $DW1 \cdot SW4 \rightarrow TW5, DW3$; the latter provides a second possible source for DW3. $TW3 \cdot SPW1 \rightarrow TW4, TW2$ serves as another possible source for TW4, which also produces TW2; this source could be active throughout the atmosphere given the pervasiveness of SPW1. TW2 can also be produced by D0 and SW2: $D0 \cdot SW2 \rightarrow TW2, DW2$, yielding DW2 as well. See Du and Ward 2010, Yue et al. 2013, and Moudden and Forbes 2013 for additional insights regarding nonmigrating terdiurnal tides from both observational and numerical modeling points of view.

Strong candidates for primary generation of semidiurnal components in the lower atmosphere include SE4, SE2, SW1, SW2, SW3, SW4, and SW6. As noted previously, it is likely that $SW2 \cdot SPW1 \rightarrow SW1, SW3$ also serves as an important source of SW1 and SW3 in both the lower and upper atmospheres (Lieberman et al. 2004; Yamashita et al. 2002; Coll and Forbes 2002; Forbes and Wu 2006; Chang et al. 2009; Liu et al. 2010). Finally, the most likely

candidate for *in situ* generation of SE1 and SE3 appears to be $SE2 \cdot SPW1 \rightarrow SE1, SE3$, but this interaction and these products remain unstudied to date in the context of numerical models.

Many of the above suggestions as to the sources of wave components can in principle be tested theoretically through numerical experiments in a general circulation model wherein various combinations of primary waves are excited within the model. This work is underway and will be reported on in the future.

Additional files

Additional file 1: Phases for Figure 6. Latitude vs. day of year variation of SABER temperature phases for migrating tidal components DW1 (top), SW2 (middle), and TW3 (bottom).

Additional file 2: Phases for Figure 7. Latitude vs. month depictions of multi-year average SABER temperature phases for DW2 at 100 km, and D0, DE2, and DE3 at 110 km.

Additional file 3: Phases for Figure 8. Latitude vs. month depictions of multi-year average SABER temperature phases for SE1, SE2, SE3, and SE4 at 110 km.

Additional file 4: Phases for Figure 9. Latitude vs. month depictions of multi-year average SABER temperature phases for SW1, SW3, SW4, and SW6 at 110 km.

Additional file 5: Phases for Figure 10. Latitude vs. month depictions of multi-year average SABER temperature phases for TE1, TW7, TW4, and TW5 at 110 km.

Additional file 6: Phases for Figure 11. Latitude vs. month depictions of multi-year average SABER temperature phases for stationary planetary wave components SPW1, SPW2, SPW3, and SPW4 at 110 km.

Competing interests
The authors declare that they have no competing interests.

Authors' contributions
AOT carried out extensive data analyses and visualizations, originally aimed at quantifying inter-annual variability, before arriving at the present results. JMF wrote the paper. XZ added some analyses and created the final figures. SEP wrote and provided the program to compute Hough functions and equivalent depths. All authors read and approved the final manuscript.

Acknowledgements
This work was supported under Grant ATM-0903179 from the National Science Foundation and Heliophysics Guest Investigator Award NNX12AJ58G from NASA, to the University of Colorado.

Received: 1 April 2014 Accepted: 29 September 2014
Published online: 30 October 2014

References
Akmaev R (2001) Seasonal variations of the terdiurnal tide in the mesosphere and lower thermosphere: a model study. Geophys Res Lett 28:3817–3820. doi:10.1029/2001GL013002

Beard AG, Mitchell NJ, Williams PJS, Kunitake M (1999) Nonlinear interactions between tides and planetary waves resulting in periodic tidal variability. J Atmos Sol Terr Phys 61:363–376

Chang LC, Palo SE, Liu H-L (2009) Short-term variation of the s = 1 nonmigrating semidiurnal tide during the 2002, stratospheric sudden warming. J Geophys Res 114:D03109. doi:10.1029/2008JD010886

Chapman S, Lindzen RS (1970) Atmospheric Tides: Thermal and Gravitational. Gordon and Breach, New York

Chau JL, Fejer BG, Goncharenko LP (2009) Quiet variability of equatorial E × B drifts during a sudden stratospheric warming event. Geophys Res Lett 36:L05101. doi:10.1029/2008GL036785

Coll AI, Forbes MJM (2002) Nonlinear interactions in the upper atmosphere: The s = 1 and s = 3 nonmigrating semidiurnal tides. J Geophys Res 107(A8):1157. doi:10.1029/2001JA900179

Du J, Ward WE (2010) Terdiurnal tide in the extended Canadian Middle Atmospheric Model (CMAM). J Geophys Res 115:D24106. doi:10.1029/2010JD014479

England SL, Immel TJ, Huba JD, Hagan ME, Maute A, DeMajistre R (2010) Modeling of multiple effects of atmospheric tides on the ionosphere: an examination of possible coupling mechanisms responsible for the longitudinal structure of the equatorial ionosphere. J Geophys Res 115:A05308. doi:10.1029/2009JA014894

Forbes JM, Garrett HB (1978) Thermal excitation of atmospheric tides due to isolation absorption by O_3 and H_2O. Geophys. Res. Lett 5:1013–1016

Forbes JM, Garrett HB (1979) Theoretical studies of atmospheric tides. Rev Geophys Space Phys 17:1951–1981

Forbes JM, Wu D (2006) Solar tides as revealed by measurements of mesosphere temperature by the MLS experiment on UARS. J Atmos Sci 63(7):1776–1797

Forbes JM, Russell J, Miyahara S, Zhang X, Palo S, Mlynczak M, Mertens CJ, Hagan ME (2006) Troposphere-thermosphere tidal coupling as measured by the SABER instrument on TIMED during July-September 2002. J Geophys Res 111:A10S06. doi:10.1029/2005JA011492

Forbes JM, Zhang X, Palo S, Russell J, Mertens CJ, Mlynczak M (2008) Tidal variability in the ionospheric dynamo region. J Geophys Res 113:A02310. doi:10.1029/2007JA012737

Forbes JM, Bruinsma SL, Zhang X, Oberheide J (2009) Surface-exosphere coupling due to thermal tides. Geophys Res Lett 36:L15812. doi:10.1029/2009GL038748

Geller MA (1970) An investigation of the lunar semidiurnal tide in the atmosphere. J Atmos Sci 27:202–218. http://dx.doi.org10.1175/1520-0469(1970)027<0202:AIOTLS>2.0.CO;2

Goncharenko L, Zhang S-R (2008) Ionospheric signatures of sudden stratospheric warming: ion temperature at middle latitude. Geophys Res Lett 35:L21103. doi:10.1029/2008GL035684

Goncharenko LP, Coster AJ, Plumb RA, Domeisen DIV (2012) The potential role of stratospheric ozone in the stratosphere-ionosphere coupling during stratospheric warmings. Geophys Res Lett 39. doi:10.1029/ 2012GL051261

Hagan ME, Forbes JM (2002) Migrating and nonmigrating diurnal tides in the middle and upper atmosphere excited by tropospheric latent heat release. J Geophys Res 107(D24):4754. doi:10.1029/2001JD001236

Hagan ME, Forbes JM (2003) Migrating and nonmigrating semidiurnal tides in the middle and upper atmosphere excited by tropospheric latent heat release. J Geophys Res 108(A2):1062. doi:10.1029/2002JA009466

Hagan ME, Roble RG (2001) Modeling diurnal tidal variability with the National Center for Atmospheric Research thermosphere-ionosphere-mesosphere-electrodynamics general circulation model. J Geophys Res 106:24869–24882

Hagan ME, Maute A, Roble RG (2009) Tropospheric tidal effects on the middle and upper atmosphere. J Geophys Res 114:A01302. doi:10.1029/ 2008JA013637

Haüsler K, Lühr H (2009) Nonmigrating tidal signals in the upper thermospric zonal wind at equatorial latitudes as observed by CHAMP. Annal Geophys 27:7,2643–2652

He M, Liu L, Wan W, Wei Y (2011) Strong evidence for couplings between the ionospheric wave structure and atmospheric tides. Geophys Res Lett 388:L14101. doi:10.1029/2011GL047855

Hendon HH, Woodberry K (1993) The diurnal cycle of tropical convection. J Geophys Res 98:16,623–637

Huang CM, Zhang SD, Fan Y (2007) A numerical study on amplitude characteristics of the terdiurnal tide excited by nonlinear interaction between the diurnal and semidiurnal tides. Earth Planets Space 59:183–191

Immel TJ, Sagawa E, England SL, Henderson SB, Hagan ME, Mende SB, Frey HU, Swenson CM, Paxton LJ (2006) Control of equatorial ionospheric morphology by atmospheric tides. Geophys Res Lett 33:L15108. doi:10.1029/2006GL026161

Immel TJ, England SL, Zhang X, Forbes JM, DeMajistre R (2009) Upward propagating tidal effects across the E and F regions of the ionosphere. Earth Planets Space 61:505–512

Jin H, Miyoshi Y, Fujiwara H, Shinagawa H (2008) Electrodynamics of the formation of ionospheric wave number 4 longitudinal structure. J Geophys Res 113:A09307. doi:10.1029/2008JA013301
Kamalabadi F, Forbes JM, Makarov NA, Portnyagin YI (1997) Evidence for nonlinear coupling of planetary waves and tides in the Antarctic mesopause. 102:4437–4446
Kil H, Oh SJ, Kelley MC, Paxton LJ, England SL, Talaat E, Min KW, Su SY (2007) Longitudinal structure of the vertical E × B drift and ion density seen from ROCSAT-1. Geophys Res Lett 34:L14110. doi:10.1029/2007GL030018
Kil H, Talaat ER, Oh SJ, Paxton LJ, England SL, Su SY (2008) Wave structures of the plasma density and vertical E × B drift in low-latitude F region. J Geophys Res 113:A09312. doi:10.1029/2008JA013106
Lieberman RS, Oberheide J, Hagan ME, Remsberg EE, Gordley LL (2004) Variability of diurnal tides and planetary waves during November 1978 - May 1979. J. Atmos. Solar-Terres. Phys 66:517–528
Lin CH, Hsiao CC, Liu JY, Liu CH (2007) Longitudinal structure of the equatorial ionosphere: time evolution of the four-peaked EIA structure. J Geophys Res 112:A12305. doi:10.1029/2007JA012455
Lindzen RS, Hong S-S (1974) Effects of mean winds and meridional temperature gradients on solar and lunar semidiurnal tides in the atmosphere. J. Atmos. Sci 31:1421–1466
Liu H-L, Roble RG (2002) A study of a self-generated stratospheric sudden warming and its mesosphericlower thermospheric impacts using the coupled TIME-GCM/CCM3. J Geophys Res 107(D23):4695. doi:10.1029/2001JD001533
Liu H, Watanabe S (2008) Seasonal variation of the longitudinal structure of the equatorial ionosphere: does it reflect tidal influences from below? J Geophys Res 113:A08315. doi:10.1029/2008JA013027
Liu H-L, Wang W, Richmond AD, Roble RG (2010) Ionospheric variability due to planetary waves and tides for solar minimum conditions. J Geophys Res 115:A00G01. doi:10.1029/2009JA015188
Moudden Y, Forbes JM (2013) A decade-long climatology of terdiurnal tides using TIMED/SABER observations. J Geophys Res Space Physics 118:4534–4550. doi:10.1002/jgra.50273
Oberheide J, Forbes JM (2008) Tidal propagation of deep tropical cloud signatures into the thermosphere from TIMED observations. Geophys Res Lett 35:L04816. doi:10.1029/2007GL032397
Pancheva DV, Mitchell NJ (2004) Planetary waves and variability of the semidiurnal tide in the mesosphere and lower thermosphere over Esrange (68°N, 21°E) during winter. J Geophys Res 109:A08307. doi:10.1029/2004JA010433
Pedatella NM, Forbes JM (2010) Evidence for stratosphere sudden warming-ionosphere coupling due to vertically propagating tides. Geophys Res Lett 37:L11104. doi:10.1029/2010GL043560
Smith AK, Ortland DA (2001) Modeling and analysis of the structure and generation of the terdiurnal tide. J Atmos Sci 58:3116–3134
Sridharan S, Sathishkumar S, Gurubaran S (2009) Variabilities of mesospheric tides and equatorial electrojet strength during major stratospheric warming events. Ann Geophys 27:4125–4130
Teitelbaum H, Vial F (1991) On tidal variability induced by nonlinear interactions with planetary waves. J Geophys Res 96:14,169–14,178
Tokioka T, Yagai I (1987) Atmospheric tides appearing in a global atmospheric general circulation model. J Meteorol Soc Jpn 65:423–437
Walterscheid RL, Venkateswaran SV (1979a) Influence of mean zonal motion and meridional temperature gradients on the solar semidiurnal atmospheric tide: a spectral study, Part 1, Theory. J Atmos Sci 36:1623–1635
Walterscheid RL, Venkateswaran SV (1979b) Influence of mean zonal motion and meridional temperature gradients on the solar semidiurnal atmospheric tide: a spectral study, Part 2, Numerical results. J Atmos Sci 36:1636–1662
Williams CR, Avery SK (1996) Diurnal nonmigrating tidal oscillations forced by deep convective clouds. J Geophys Res 101:4079–4091
Yagai I (1989) Nonmigrating thermal tides detected in data analysis and a general circulation model simulation. J Geophys Res 94:6341–6356
Yamashita K, Miyahara S, Miyoshi Y, Kawano K, Ninomiya J (2002) Seasonal variation of nonmigrating semidiurnal tide in the polar MLT region in a general circulation model. J Atmos Solar-Terr Phys 64:1083–1094
Yue J, Xu J, Chang LC, Wu Q, Liu H, Lu X, Russell J (2013) Global structure and seasonal variability of the migrating terdiurnal tide in the mesosphere and lower thermosphere. J Atmos Solar-Terr Phys:191–198. doi:10.1016/j.jastp.2013.10.010
Zhang X, Forbes JM, Hagan ME (2010a) Longitudinal variation of tides in the MLT region: 1. Tides driven by tropospheric net radiative heating. J Geophys Res 115:A06316. doi:10.1029/2009JA014897
Zhang X, Forbes JM, Hagan ME (2010b) Longitudinal variation of tides in the MLT region: 2. Relative effects of solar radiative and latent heating. J Geophys Res 115:A06317. doi:10.1029/2009JA014898

doi:10.1186/s40623-014-0136-4
Cite this article as: Truskowski *et al.*: New perspectives on thermosphere tides: 1. Lower thermosphere spectra and seasonal-latitudinal structures. *Earth, Planets and Space* 2014 **66**:136.